



# Study on angular distribution of differential photoacoustic cross-section and its implication in source size determination

ANUJ KAUSHIK, DEEPAK SONKER, AND RATAN K. SAHA\*

Department of Applied Sciences, Indian Institute of Information Technology Allahabad, Jhalwa, Allahabad 211015, India

\*Corresponding author: ratank.saha@iiita.ac.in

Received 21 November 2018; revised 21 January 2019; accepted 21 January 2019; posted 22 January 2019 (Doc. ID 352520); published 22 February 2019

Angular distribution of a differential photoacoustic cross-section (DPACS) has been examined for various non-spherical axisymmetric particles. The DPACS as a function of measurement angle has been computed for spheroidal particles with varying aspect ratios and fitted with a tri-axes ellipsoid form factor model to extract shape parameters. Similar study has been carried out for normal and pathological red blood cells, and fitting has been performed with the tri-axes ellipsoid and finite cylinder form factor models to evaluate cellular morphology. It is found that an enhancement of the DPACS occurs as the surface area of the photoacoustic source normal to the direction of measurement is increased. It decreases as the thickness of the source along the same direction increases. For example, the DPACS for normal erythrocyte along the direction of symmetry is nearly 20 times greater than a pathological cell. Further, the first minimum appears slightly later ( $\approx 4^\circ$ ) for a healthy cell compared with that of a diseased cell. Shape information of spheroids can be precisely estimated by the first model. Both models provide accurate estimates of shape parameters for normal red blood cells (errors within 4%). It may be possible to assess cellular morphology from an angular profile of the DPACS using form factor models. © 2019 Optical Society of America

<https://doi.org/10.1364/JOSAA.36.000387>

## 1. INTRODUCTION

Photoacoustic (PA) imaging is a nonionizing, noninvasive, and hybrid imaging modality. In this technique, a tissue is illuminated by a nanosecond pulsed laser. It absorbs light energy, gets heated, and exhibits thermoelastic expansion releasing broadband acoustic waves [1]. Microscopy and tomography techniques have been developed over the last two decades, exploiting the PA effect [2,3]. The major advances of this technique are as follows: (i) high-contrast images can be formed at ultrasonic resolution because endogenous/exogenous chromophores produce PA signals and nonabsorbing tissue components do not emit any background signal, (ii) imaging at a depth of several centimeters with a resolution of a few hundred micrometers is possible because both ballistic and diffusion photons contribute to the generation of the PA signals, and (iii) it has the ability to construct functional images by selectively exciting chromophores at two/three optical wavelengths followed by a simple spectroscopic analysis. The PA imaging technique has been used to visualize small animal vasculature, brain hemodynamics, blood oxygen saturation, and hemoglobin concentration [2,3]. The PA method is also one of the fastest-growing techniques for molecular imaging [4,5].

Recent works in this field have demonstrated that single cell imaging is possible using the PA microscopy for visible or near-infrared input light [6–8]. This technique does not need any labeling and therefore can be used to image live red blood cells (RBCs), melanoma cells, etc. These cells contain endogenous contrast agents such as hemoglobin and melanin, respectively, and hence produce acoustic signals upon light absorption. However, it is difficult to obtain information of their size and shape from the PA images. Strohm et al. further showed that PA spectral features are related to the size and shape of cells under investigation [7,8]. Therefore, it may be feasible to assess cellular morphology by analyzing experimental PA signals in the frequency domain. Theoretical studies can also be carried out to gain insight into how physical and morphological properties of cells affect PA spectral features. Previously, we calculated a PA signal from a single RBC assuming as a sphere by solving the PA wave equation in the frequency domain using the exact method [9]. The model was successively explored to study the effects of RBC aggregation and oxygenation on a PA signal [10,11]. PAs of malaria-infected RBCs and melanoma cells in blood have been examined by exploiting this model, too [12,13]. Experiments were also conducted to examine

the effects of RBC aggregation and hemolysis of RBCs on PA signals [14,15].

The exact method cannot work for irregular shapes. To overcome this limitation, Li *et al.* recently developed methods for calculating the PA signals from spheroidal droplets [16,17]. This method uses a spheroidal coordinate system, and the corresponding mathematical formulation is not straightforward. PA signals from sources with arbitrary geometries can be simulated using the k-Wave simulation toolbox [18], which is a widely used free software. It implements a pseudospectral method to solve the PA wave equation. Recently, we adopted Green's function method to solve the PA wave equation and, accordingly, defined a quantity called the differential photoacoustic cross-section (DPACS) [19]. It is defined as the acoustic power received per unit solid angle divided by the intensity of the incident light beam. Green's function technique in general provides closed-form solutions for regular objects (e.g., sphere, cylinder), and numerical solutions can be obtained for irregular objects. Variation of the PA spectral power (which is proportional to the DPACS) for various particles, including normal and deformed RBCs, have been studied extensively over a wide-frequency range (10–1000 MHz) [19]. It was shown that the locations of frequency minima depend on the width of the PA source along the direction of measurement. Uluc *et al.* developed a robust transport model for characterization of RBC morphology in microchannel flow [20]. The authors coupled the Navier–Stokes and the PA wave equations to study effects of many factors such as deformability (plasma viscosity, plasma density, intercellular interaction) and laser parameters (beam-width, pulse duration, etc.) on single-cell PA emission. It may be mentioned here that the evaluation of RBC deformation is of profound interest from the clinical point of view. Deformation of RBCs occurs greatly in the case of malaria and sickle cell anemia and induces circulatory disorder significantly [21,22].

The objective of the paper is to study how the DPACS varies with angle of measurement for different shapes. In this forward problem formulation, we computed angular patterns of the DPACS for spheroidal droplets and normal and deformed RBCs. The first class of particles has been considered because it is simple and widely used in other studies. The second set of corpuscles may be interesting from the application point of view. Surface parametrization with the Legendre polynomial expansion has also been performed for RBCs as well. It is shown that magnitude of the DPACS increases as the surface area of the PA source normal to the direction of measurement increases. Moreover, it decreases as the width of the particle along the direction of measurement increases. The form factor models have been extensively used in light, X-ray, and neutron-scattering problems to estimate scatter size [23–25]. It is accomplished by fitting angular distribution of differential scattering cross-section with a suitable form factor model. An attempt has been made in this work as well to estimate the size of the PA source from angular distribution of the DPACS using tri-axes ellipsoid and finite cylinder form factor models. The numerical results demonstrate that characteristic size can be obtained accurately for regular objects (e.g., ellipsoid). The inverse frameworks provide best estimates for morphological parameters of normal RBC.

The organization of the paper is as follows. The next section details the definition of the DPACS. It also describes different shapes considered in this study. The form factor models and size estimation procedure are described in this section too. The numerical results illustrating angular distributions of the DPACS for various nonspherical axisymmetric shapes are presented in Section 3. The results are also discussed in Section 3. The conclusions are drawn in Section 4.

## 2. MATERIALS AND METHODS

### A. Derivation of the PA Field

The mathematical expressions for the PA wave equation, its solution, and DPACS are given in detail in previous publications [19,26]. However, for the sake of completeness, pertinent equations are presented here in brief. The broadband PA pulse generated by tissue upon absorption of electro-magnetic radiation is governed by the inhomogeneous wave equation as [9]

$$\nabla^2 p - \frac{1}{v^2} \frac{\partial^2 p}{\partial t^2} = -\frac{\beta}{C_p} \frac{\partial H}{\partial t}, \quad (1)$$

where  $\beta$  is the thermal expansion coefficient,  $C_p$  is the specific heat capacity,  $v$  is the speed of sound for the absorbing region, and  $H$  is a function that describes heating of the sample per unit time and volume. The condition of thermal confinement is included during the derivation of the above equation. If the optical radiation of intensity  $I_0$  propagates along the  $x$  axis and varies sinusoidally with time, then the heating function can be expressed as

$$H(x, t) = \mu(x) I_0 e^{-i\omega t}, \quad (2)$$

where  $\mu(x)$  is the light absorption coefficient of the illuminated region and  $\omega$  is the modulation frequency of the laser beam. Equation (2) indicates that the light absorption coefficient varies along the  $x$  direction. However, it may in general vary along all three dimensions depending upon the spatial distribution of permittivity (or refractive index) of the medium. The steady-state pressure can be written for a homogeneous absorber as

$$\nabla^2 p + k^2 p = \begin{cases} \frac{i\omega\mu\beta I_0}{C_p}, & \text{inside the absorber} \\ 0, & \text{outside the absorber} \end{cases}, \quad (3)$$

with  $k$  as the wavenumber of the acoustic wave. The solution to Eq. (3) can be obtained as

$$p_{\text{ext}}(\mathbf{r}, k) = \int A G(\mathbf{r}|\mathbf{r}_0) d^3 \mathbf{r}_0, \quad (4)$$

where  $A = \frac{i\omega\mu\beta I_0 \omega}{C_p}$  and  $G(\mathbf{r}|\mathbf{r}_0)$  is the free space Green's function, and  $\mathbf{r}(r, \theta, \phi)$  and  $\mathbf{r}_0(r_0, \theta_0, \phi_0)$  denote field and source points, respectively. A schematic diagram is shown in Fig. 1. The subscript ext indicates that the field point is outside the absorbing region (i.e.,  $r > r_0$ ). The free space Green's function satisfies [27]

$$\nabla^2 G(\mathbf{r}|\mathbf{r}_0) + k^2 G(\mathbf{r}|\mathbf{r}_0) = \delta(\mathbf{r} - \mathbf{r}_0) \quad (5)$$

and is given by

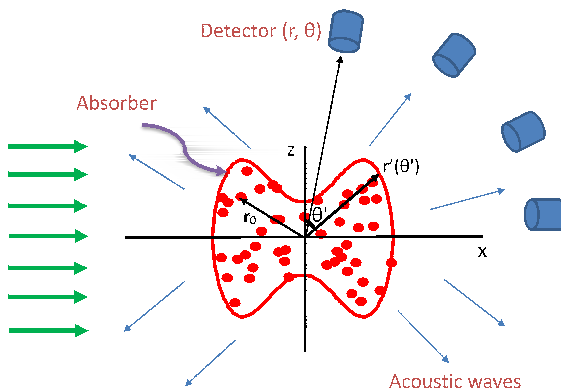


**Fig. 1.** Demonstration of PA wave generation from an erythrocyte.

$$G(\mathbf{r}|\mathbf{r}_0) = -\frac{e^{ik|\mathbf{r}-\mathbf{r}_0|}}{4\pi|\mathbf{r}-\mathbf{r}_0|}. \quad (6)$$

Here, we consider a simple situation that a source has an impedance matching with its surrounding medium. In the far field ( $r \gg r_0$ ), Green's function can be approximated as  $G(\mathbf{r}|\mathbf{r}_0) \approx -(1/4\pi r)e^{ikr}e^{-ik\cdot\mathbf{r}_0}$  with  $\mathbf{k}$  as the direction of measurement; thus, Eq. (4) becomes

$$p_{\text{ext}}(\mathbf{r}, k) \approx -\frac{e^{ikr}}{4\pi r} \int A e^{-ik\cdot\mathbf{r}_0} d^3\mathbf{r}_0 = \frac{e^{ikr}}{r} M(\mathbf{k}), \quad (7)$$

where

$$M(\mathbf{k}) = -\frac{1}{4\pi} \int A e^{-ik\cdot\mathbf{r}_0} d^3\mathbf{r}_0. \quad (8)$$

It may be noted that  $M(\mathbf{k})$  denotes the amplitude of the outgoing spherical wave emitted by the PA source.

## B. Derivation of the Differential PA Cross-Section

The differential scattering cross-section is a well-defined quantity, which has been computed and measured in various branches of science and engineering to study scattering properties of inhomogeneities. An analogous expression for the PA emission can be deduced. Let us define a quantity called the DPACS (i.e., acoustic power per unit solid angle received far away from the PA source divided by the intensity of light beam), which can be expressed as [19,26]

$$\sigma(k, \theta) = \frac{|M(\mathbf{k})|^2}{2\rho v I_0}. \quad (9)$$

Here,  $\rho$  is density of the surrounding medium. The total PA cross-section can readily be calculated by integrating  $\sigma(k, \theta)$  over the entire solid angle. The total PA cross-section can be interpreted as a hypothetical area, and light energy of which converts into acoustic energy due to the PA effect. For a regular object, integration in Eq. (8) can be calculated analytically providing a closed-form expression for  $\sigma(k, \theta)$ . For instance, for a homogeneous spherical absorber, Eq. (9) reduces to [19,26]

$$\sigma(k, \theta) = \frac{\mu^2 \beta^2 I_0 v}{2\rho C_P^2} q^4 [j_1(kq)]^2, \quad (10)$$

where  $j_1$  is the spherical Bessel function of order unity and  $q$  is the radius of the spherical absorber. For an irregular PA source,

it is not possible to yield an analytical solution; however, a numerical solution can be obtained for the DPACS. In this work, we calculate Eq. (9) as a function of measurement angle  $\theta$ , as shown in Fig. 1 for different nonspherical axisymmetric particles such as spheroidal droplets and RBCs.

## C. Derivation of the Form Factor

The DPACS as given in Eq. (10) can also be written as

$$\begin{aligned} \sigma(k, \theta) &= \frac{\mu^2 \beta^2 I_0 v}{2\rho C_P^2} q^4 [j_1(kq)]^2 \\ &= \frac{\mu^2 \beta^2 I_0 \omega^2}{2\rho v C_P^2} \frac{q^6 [3j_1(kq)]^2}{9 k^2 q^2} \\ &= \frac{\mu^2 \beta^2 I_0 \omega^2}{2\rho v C_P^2} \frac{V_{\text{vol}}^2}{16\pi^2} FF^2, \end{aligned} \quad (11)$$

where

$$FF = \frac{3j_1(kq)}{kq} \quad (12)$$

is known as the form factor (in this case it is a spherical form factor). Here,  $V_{\text{vol}}$  denotes the volume of the spherical absorber [for a nonspherical absorber the second factor,  $\frac{V_{\text{vol}}^2}{16\pi^2}$  in Eq. (11), will have a different form]. Note that  $FF \rightarrow 1$  when  $kq \rightarrow 0$ ; therefore,  $\sigma(k, \theta)$  will not be a function of  $\theta$  for a point PA source. In other words, the DPACS will be independent of its shape. For a PA source with finite size, the form factor exhibits variation with angle and hence dictates how  $\sigma(k, \theta)$  will vary with  $\theta$ .

In Eq. (11), we have used a spherical form factor; however, several other form factor models are also available in the literature [23–25]. For example, a tri-axes ellipsoid form factor is expressed as [23]

$$FF = \frac{3j_1(k'q_1)}{k'q_1}, \quad (13)$$

where  $q_1, q_2$ , and  $q_3$  are the semi-axes of the ellipsoid and  $k' = \frac{k}{q_1} (q_1^2 \sin^2 \theta \cos^2 \phi + q_2^2 \sin^2 \theta \sin^2 \phi + q_3^2 \cos^2 \theta)^{\frac{1}{2}}$ . The finite cylinder form factor is given by [23,25]

$$FF = \frac{2J_1(k\Gamma \sin \theta) \sin[(kL \cos \theta)/2]}{k\Gamma \sin \theta} \frac{(kL \cos \theta)/2}{(kL \cos \theta)/2}, \quad (14)$$

where  $\Gamma$  and  $L$  are the radius and length of the cylinder, respectively. In this work, the form factor models have been used to obtain size and shape information of the PA source from angular distribution of the DPACS.

## D. Nonspherical Axisymmetric PA Sources

### 1. Spheroidal Droplets

A spheroid can be generated by rotating an ellipse either about its major axis or its minor axis. Accordingly, they are known as prolate and oblate spheres, respectively. The radial distance of a point on the surface of such an object is given by (see Fig. 1)

$$r'(\theta') = \frac{ab}{[b^2 \sin^2 \theta' + a^2 \cos^2 \theta']^{1/2}}, \quad (15)$$

with  $a$  and  $b$  are the semi-axes. For prolate sphere  $b > a$  and for oblate sphere  $b < a$ . Two representative shapes of spheroidal

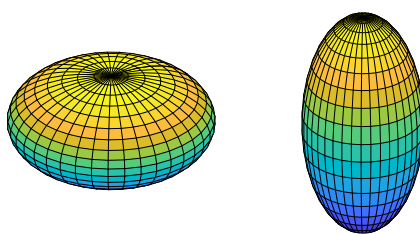


**Fig. 2.** Spheroidal droplets with  $b:a = 1:2$  (left panel) and  $b:a = 2:1$  (right panel).

droplets are shown in Fig. 2. In this work, we have studied how the angular distribution of the DPACS changes for different spheroidal droplets.

## 2. Red Blood Corpuscles

A normal RBC looks like a biconcave disk, which is axially symmetric. It is really thin at the center but slightly thicker at the edge. This particular shape maximizes surface-to-volume ratio and helps to perform physiological functions [28]. There are many agents that can alter the normal shape of RBCs [29,30]. Two common forms of pathological shapes are echinocyte and stomatocyte. In the case of echinocyte, many equally spaced similar protrusions projecting outward are observed to exist. Stomatocytes are axisymmetric- and concave-shaped cells. In this study, we will restrict ourselves to axisymmetric shapes, which can be obtained by rotating the following curve [19],

$$r'(\theta') = R_e \left[ 1 + \sum_n \alpha_n P_n(\cos \theta') \right], \quad (16)$$

about an axis passing through  $\theta' = 0$ . Here,  $R_e$  is the radius of a spherical envelope that encloses RBC,  $\alpha$  is the parameter that controls shape, and  $P_n$  is the Legendre polynomial of degree  $n$ . The Legendre polynomials are orthogonal basis functions and form a complete set of basis functions. Any arbitrary function within  $0 \leq \theta \leq \pi$  can be expanded in terms of these basis functions. In this work, this expansion was used to generate shapes for normal RBC and pathological RBCs mimicking stomatocytes. Angular distribution of the DPACS has been computed for such cells.

## E. Simulation Parameters

### 1. Physical Parameters

The density and speed of sound for the PA source were taken as  $\rho = 1005 \text{ kg/m}^3$  and  $v = 1498 \text{ m/s}$ , respectively. The same numerical values were also considered for the surrounding medium. Further, specific heat capacity and thermal expansion coefficient for the absorbing region were chosen as  $C_p = 3.23 \times 10^3 \text{ J kg}^{-1} \text{ K}^{-1}$  and  $\beta = 1.5 \times 10^{-4} \text{ J kg}^{-1} \text{ K}^{-1}$ , respectively [31]. The intensity of the light beam was fixed to  $I_0 = 1.51 \times 10^{12} \text{ J m}^{-2} \text{ s}^{-1}$ . This value was calculated by dividing fluence with the pulse width [7]. The optical absorption coefficient for RBC was calculated using the formula  $\mu = 2.303\epsilon c_{\text{Hb}}$  and found out to be  $809.02 \text{ m}^{-1}$  at 798 nm ( $\epsilon$  is the molar extinction coefficient and  $c_{\text{Hb}}$  is the molar concentration of hemoglobin). It was assumed that each RBC approximately contains 280 million hemoglobin molecules, and light

absorption by oxy- and deoxy-hemoglobin molecules is the same at this wavelength [32,33]. This value was also used for spheroidal particles. The numerical values for these parameters are summarized in Table 1.

## 2. Shape Parameters

In this work, we considered seven different spheroidal droplets. The aspect ratio varied from 8:1 to 1:8; however, the volume remained fixed at  $\approx 524 \mu\text{m}^3$  for each particle. This volume corresponded to a sphere of radius 5  $\mu\text{m}$ . Details of shape parameters of these particles are given in Table 2.

Various parametric models are available in the literature to theoretically construct RBC shape [28]. Some commonly used models with three or more degrees of freedom include the Evans–Fung model, Kuchel–Fackrell model, and Yurkin model. In this work, we rely on the Cassini oval, which can be cast as [34]

$$(x^2 + y^2 + z^2 + \eta^2)^2 - 4\eta^2(x^2 + y^2) = \zeta^4. \quad (17)$$

It has two degrees of freedom. It has been observed that the biconcave shape can be reproduced from Eq. (17) when  $\eta$  is slightly less than  $\zeta$ . Further, the numerical values of  $\eta$  and  $\zeta$  can be determined from four morphological parameters, namely, diameter ( $D$ ), dimple thickness ( $t$ ), maximum thickness ( $h$ ), and the diameter of the circular contour drawn on the location of the maximum thickness ( $d$ ) {see Fig. 1(b) of [28]} because they are related as  $D^2 = 4(\zeta^2 + \eta^2)$ ,  $t^2 = 4(\zeta^2 - \eta^2)$ , and  $h = \zeta^2/\eta$ . Typical values of morphological parameters corresponding to normal RBC are listed in Table 2 (rows 3 and 4). Two shapes mimicking stomatocytes (Stomatocyte1 and Stomatocyte2) were produced by varying these morphological parameters phenomenologically. For these shapes, the upper half was generated using Eq. (17); however, the lower part was assumed to be a half-sphere. The Cassini parameters (in  $\mu\text{m}$ ) were computed to be  $\eta = 2.66, 2.04, 2.31$  and  $\zeta = 2.75, 2.45, 2.32$ , respectively, for three shapes.

**Table 1. Numerical Values for Physical Parameters Used in Computation**

$\rho$	1005 $\text{kg/m}^3$
$v$	1498 $\text{m/s}$
$\mu$	$809.02 \text{ m}^{-1}$
$\beta$	$1.5 \times 10^{-4} \text{ K}^{-1}$
$C_p$	$3.23 \times 10^3 \text{ J kg}^{-1} \text{ K}^{-1}$
$I_0$	$1.51 \times 10^{12} \text{ J m}^{-2} \text{ s}^{-1}$

**Table 2. Numerical Values for Shape Parameters Used in Calculation (Unit for Length Parameters Is in  $\mu\text{m}$ )**

Objects	Volume ( $\mu\text{m}^3$ )	Shape Parameters
Spheroids	523.6	$b:a = 1:8, 1:4, 1:2, 1:1, 2:1, 4:1, 8:1$
RBCs	104	$D = 7.65, t/2 = 0.70, h/2 = 1.42, R_e = 0.5D, d = 0.7D, L = 19$
	105	$D = 6.37, t/2 = 1.36, h/2 = 1.47, R_e = 0.5D, d = 0.7D, L = 19$
	104	$D = 6.54, t/2 = 0.21, h/2 = 1.16, R_e = 0.5D, d = 0.7D, L = 19$

Theoretically constructed shapes were then fitted with the expansion given in Eq. (16) in order to estimate  $\alpha_n$ . At first, we generated  $s$  number of radial samples (i.e.,  $r_1, r_2 \dots r_s$ ) at different angular locations ( $\theta_1, \theta_2 \dots \theta_s$ ). Then, we constructed a system of equations considering up to the  $L$ th deg Legendre polynomial as [see Eq. (16)]

$$\begin{pmatrix} P_0(\gamma_1) & P_1(\gamma_1) & \dots & P_L(\gamma_1) \\ P_0(\gamma_2) & P_1(\gamma_2) & \dots & P_L(\gamma_2) \\ \vdots & \vdots & \ddots & \vdots \\ P_0(\gamma_s) & P_1(\gamma_s) & \dots & P_L(\gamma_s) \end{pmatrix} \begin{pmatrix} \alpha_0 \\ \alpha_1 \\ \vdots \\ \alpha_L \end{pmatrix} = \begin{pmatrix} \frac{r_1}{R_e} - 1 \\ \frac{r_2}{R_e} - 1 \\ \vdots \\ \frac{r_s}{R_e} - 1 \end{pmatrix}, \quad (18)$$

where  $\gamma_1 = \cos \theta_1, \gamma_2 = \cos \theta_2, \dots, \gamma_s = \cos \theta_s$ . The above equations have been solved using the least-square fitting technique for obtaining  $\alpha_n$ s. In this work, we generated more than 181 radial samples, and the infinite sum in Eq. (16) was truncated at  $L = 19$ , which was fixed based on the literature [35,36]. Simulated 3D shapes are shown in Fig. 3 (upper panel), and associated  $\alpha$  vectors are also plotted in Fig. 3 (lower panel).

#### F. Computation of the DPACS

The amplitude of the PA field at a distance  $r = 1$  mm generated by a source was obtained by evaluating the integration in Eq. (8). The Monte Carlo integration method was implemented for this purpose [37]. Essentially, a large number of points were randomly thrown within a rectangular box that enclosed the PA source of interest. The points/throws located inside the source only contributed to the field calculation. For example, a box of size  $V_b = 11 \times 11 \times 11 \mu\text{m}^3$  was chosen to bound a spherical particle of radius 5  $\mu\text{m}$ . A total number of  $N_T = 5 \times 10^6$  points were thrown inside the box, and the number of throws within the spherical shape was counted to be  $N_{\text{In}} \approx 2 \times 10^6$ . The fields generated by such a point source at 181 detector positions were computed and stored in an array. After that, fields for individual points inside the PA source were

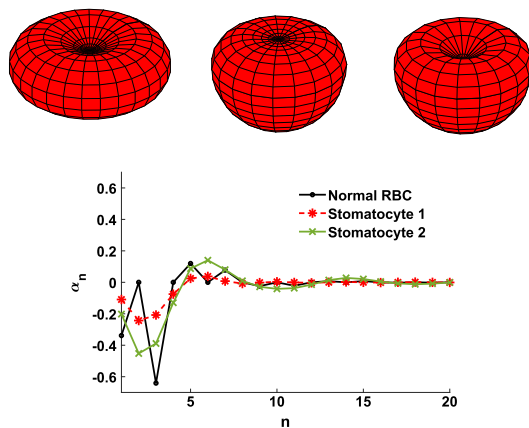


**Fig. 3.** Visualization of normal and pathological RBCs in 3D (normal RBC top row, left panel; Stomatocyte1 top row, middle panel; Stomatocyte2 top row, right panel). Plots of  $\alpha$  vectors (bottom row).

evaluated for each detector position and summed up to obtain the resultant field. The average infinitesimal volume element could be found out to be  $d^3 \mathbf{r}_0 \approx V_b/N_T$ . The DPACS was calculated as a function of polar angle ( $\theta$ ). This means that the 181 detectors were placed from 0 to  $180^\circ$  with a separation of  $1^\circ$ . The execution time to determine the DPACS at 181 angular locations was estimated to be  $\approx 30$  s in a personal computer (OS, Window 10; RAM, 12 GB; i5 processor; 3.50 GHz, clock speed). A large number of Monte Carlo throws was considered in this study to obtain converging results.

The PA signals from normal and infected RBCs were also computed using the k-Wave toolbox. This step was performed to qualitatively validate results generated by Green's function approach for RBCs. Computational grid size was taken as  $256 \times 256 \times 256$  with a resolution of  $0.1 \mu\text{m}$ , and a perfectly matched layer of the thickness of 20 grid points was attached to the computational domain from outside. The PA source of interest was placed at the center of the computational grid, and signals were recorded by 181 points detectors uniformly located between  $\theta = 0-180^\circ$ . Each detector was positioned at a distance of  $12 \mu\text{m}$  from the center. The PA power at 390 MHz was computed for each shape and plotted as a function of measurement angle for comparison. This simulation was carried out in a workstation (OS, Linux; RAM, 32 GB; Xeon processor; 2.10 GHz, clock speed). The computational time was about 2 h and 30 min.

#### G. Size Estimation from Angular Distribution of the DPACS Using Form Factor Models

As stated earlier, various form factor models have been used in light, x-ray, and neutron scattering problems to fit the angular distribution of differential scattering cross-section data and, accordingly, to determine scatter size. In this work, we also performed a similar analysis. At first, angular location at which the DPACS became maximum was identified (let  $\theta_m$ ); then, a normalized spectrum was obtained as  $\sigma(k, \theta)/\sigma(k, \theta_m)$ . An identical step was also executed for the form factor [i.e.,  $\text{FF}(k, \theta)/\text{FF}(k, \theta_m)$ ]. The next step was to iteratively vary the fitting parameters (e.g.,  $Q_1, Q_2, Q_3$  in the case of the tri-axes ellipsoid model and  $\Gamma, L$  in the case of the finite cylinder model) and minimize the following cost function:

$$\Omega = \left\| 10 \log_{10} \left[ \frac{\sigma(k, \theta)}{\sigma(k, \theta_m)} \right] - 10 \log_{10} \left[ \frac{\text{FF}^2(k, \theta)}{\text{FF}^2(k, \theta_m)} \right] \right\|^2, \quad (19)$$

where  $\|\cdot\|$  refers to the Euclidean norm. Note that the total error between the simulated (normalized) and fitted curves was computed over a range of  $\theta_m$  to the first minimum in the increasing  $\theta$  direction. The set of parameters with minimum fitting error provided characteristic dimensions of the PA source along different directions. In this work, the tri-axes ellipsoid form factor model was used to fit the DPACS data corresponding to ellipsoids. However, both the tri-axes ellipsoid and the finite cylinder models were utilized to fit the DPACS data for RBCs.

### 3. RESULTS AND DISCUSSION

Plots of the DPACS calculated at 200 MHz (wavelength,  $\lambda \approx 7.5 \mu\text{m}$ ) as a function of polar angle ( $\theta$ ) for oblate spheres are shown in Fig. 4(a). The variation of the radius with an angle

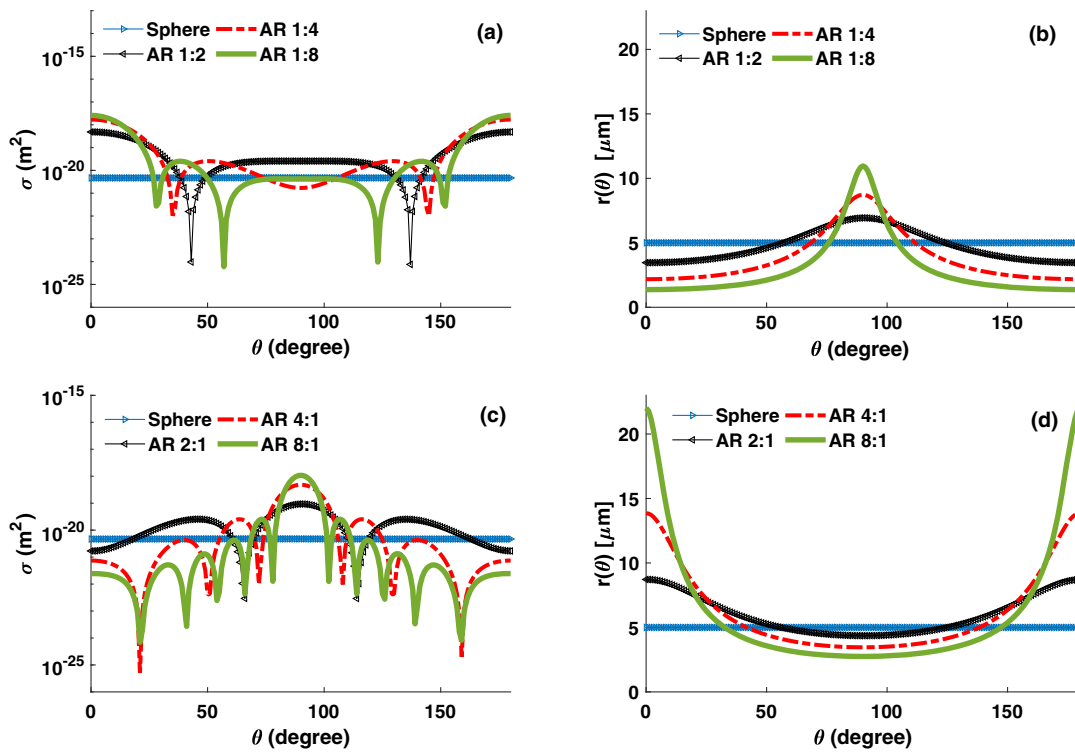
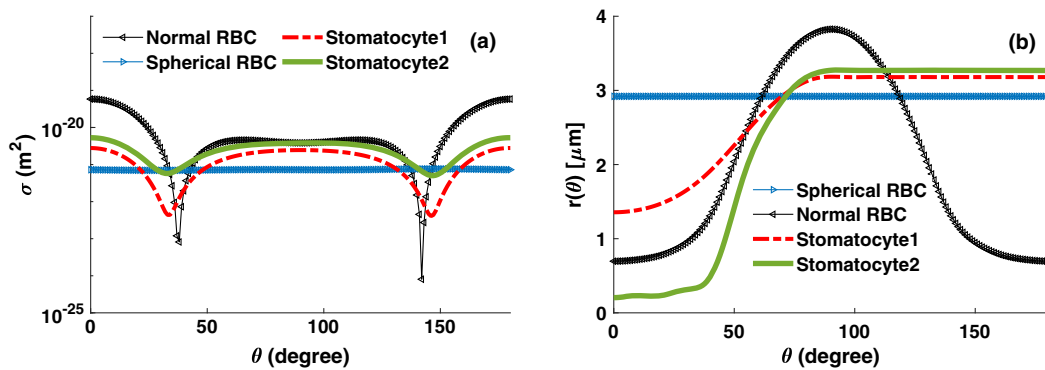


**Fig. 4.** (a) Angular distribution of the DPACS for oblate spheroids computed at 200 MHz for 798 nm incident optical illumination. (b) Angular profile for radius for each object. (c) and (d) Same as (a) and (b), respectively, but for prolate spheroids. AR stands for aspect ratio.

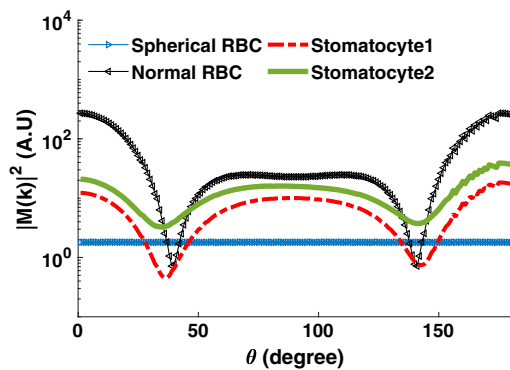
for each object is presented in Fig. 4(b). The DPACS for a spherical droplet with 5  $\mu\text{m}$  radius is also plotted in the same figure for ready reference. It remains constant throughout the angular domain considered in this study because a spherical source acts as a monopole source. For oblate spheres,  $\sigma$  becomes maximum at  $\theta = 0$  and then passes through successive maxima and minima. The heights of maxima gradually decrease as  $\theta$  increases from 0 to  $\pi/2$  for each line. The angular interval between two successive maxima/minima decreases as the aspect ratio increases. Further, the first minimum appears earlier for the curve with a higher aspect ratio than that of the lower aspect ratio. For example, the first minimum for a particle with  $b:a = 1:8$  nearly occurs at 28° but that of  $b:a = 1:2$  arises around 43°. It can be noted that  $\sigma$  is symmetric with respect to  $\theta = \pi/2$ . This is expected because the PA sources are symmetric with respect to the  $z = 0$  plane. Similar graphs for prolate spheres over the entire angular regime are displayed in Fig. 4(c), and an angular variation of the radius of those objects is shown in Fig. 4(d). Each line exhibits well-known peak and dip patterns. Additionally,  $\sigma$  values at the locations of maxima grow with increasing measurement angle and attain the maximum at  $\theta = \pi/2$ . The number of oscillations increases as the aspect ratio is increased, as we have observed in Fig. 4(a). It may be noted that Figs. 4(a) and 4(b) in general vary in a complementary manner, meaning that the DPACS becomes maximum when  $r(\theta)$  approaches minimum and *vice versa*. The same is true for Figs. 4(c) and 4(d). In other words, Fig. 4 reveals that the magnitude of the DPACS at an angular location depends upon the geometrical cross-sectional area of the source exposed to that direction.

Figure 5(a) illustrates how the DPACS varies with  $\theta$  for different RBCs, and the angular profile for radius for each cell is shown in Fig. 5(b). In this case, we considered 400 MHz, which corresponded to a wavelength of  $\approx 3.75 \mu\text{m}$ . The plot of  $\sigma$  for the equivalent sphere (of radius 2.92  $\mu\text{m}$ ) is also included in this figure for comparison. Note that, for normal RBC, the computed value of the DPACS at  $\theta = 0^\circ$  is significantly greater than that of  $\theta = \pi/2$ . This shape has generated only one minimum, which has appeared nearly at 38°. The line remains flat over a large angle from  $\theta = 50^\circ$  to  $90^\circ$ . It is symmetric with respect to  $\theta = \pi/2$  because its radial profile is symmetric, as shown in Fig. 5(b). Computed values of  $\sigma$  for Stomatocyte1 and Stomatocyte2 are shown in this figure over the entire angular domain. Both curves follow an identical trend. The curve corresponding to Stomatocyte1 exhibits a dip at 34°, which is slightly earlier than that of the normal erythrocyte. However, the same for Stomatocyte2 is not so prominent. As in the previous case, the line for the DPACS for each deformed RBC looks symmetric with respect to  $\pi/2$ . This may be due to the fact that the thickness profile is approximately symmetric for both cases, as shown in Fig. 5(b). The DPACS for normal RBC is approximately 1 order of magnitude higher than that of pathological RBCs when it is measured along the symmetry axis. This is because the surface area of the healthy RBC perpendicular to the  $z$  axis is larger than that of diseased RBCs.

The angular pattern of the PA signal power has also been examined using the k-Wave toolbox for RBCs. Simulation results at 390 MHz are displayed in Fig. 6 over the whole angular range. It can be seen that the PA signal power for normal RBC is significantly higher than pathological RBCs at 0°.



**Fig. 5.** (a) Plots of the DPACS as a function of  $\theta$  for normal and pathological RBCs at 400 MHz for 798 nm exciting radiation. (b) Angular variation of radius for each cell.



**Fig. 6.** Plots of the PA spectral power computed at 390 MHz as a function of  $\theta$  for normal and deformed RBCs using the k-Wave toolbox.

Minima positions for infected RBCs appear slightly ahead of the normal erythrocyte. These are consistent with Fig. 5(a). However, little quantitative disagreement between the two approaches may be noticed. For example, the curves for normal RBC and Stomatocyte2 are overlapping at  $90^\circ$  in Fig. 5(a), but they are not overlapping in Fig. 6. The PA fields in the former method were computed at  $r = 1000 \mu\text{m}$ , but, in the latter procedure, it was  $12 \mu\text{m}$ . Little quantitative difference might have occurred due to this mismatch. Overall qualitative agreement between Figs. 5(a) and 6 validates the Green's function results.

Normalized DPACSS as a function of  $\theta$  are plotted in Fig. 7(a) for oblate spheres. The corresponding best-fitted curves based on the tri-axes ellipsoid form factor model are also presented in the same figure over the entire angular range. The model provides excellent fit to the normalized curves, and the corresponding evaluated parameters are presented in Table 3 (rows 4–12). The angular range over which fitting was performed for each case, and associated fitting error as a measure of goodness of fit are also given in this table. It can be seen that numerical values of  $q_1$  and  $q_3$  are accurately estimated when the DPACS data are fitted along the  $\phi = 0^\circ$  direction (compare Rows 4 and 6 of Columns 2 and 4). However,  $q_2$  and  $q_3$  are correctly predicted when  $\phi = 90^\circ$  (compare Rows 5 and 6 of Columns 2 and 5). Figure 7(b) demonstrates normalized graphs for prolate spheroids. The best-fitted curves are included in the same figure as well. In this case, the model also facilitates exact fits to the curves, and that is why estimates are accurate, as appended in Table 3 (Rows 13–21).

Plots of normalized DPACSS are shown in Fig. 8 for RBCs. Best-fitted curves for the tri-axes ellipsoid and the finite cylinder form factor models are displayed in the same figure as well. Numerical values for the fit parameters and fitting errors are given in Table 4. Both the models provide good fits to the simulated data over the entire angular domain, as shown in the top panel of Fig. 8 (the finite cylinder form factor model seems to be marginally inferior near  $\theta = 90^\circ$ ). Table 4 (Rows 4–6 and Columns 4 and 5) demonstrates that the predicted values of  $q_1$

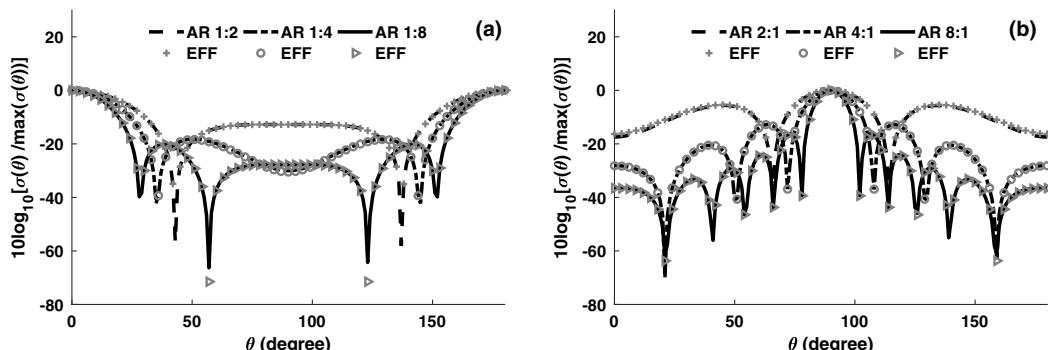


**Fig. 7.** Fitting of the angular distribution of the DPACS with the tri-axes ellipsoid form factor model for each oblate spheroid in (a) and prolate spheroid in (b). Here, EFF refers to the tri-axes ellipsoid form factor.

**Table 3.** Comparative Study between the Nominal Values of the Morphological Parameters of the Spheroids Considered in This Study and the Estimated Values of the Semi-axes along the  $x$ ,  $y$ , and  $z$  Directions, Respectively<sup>a</sup>

PA Source Spheroid	Nominal Values ( $\mu\text{m}$ )	Angular Range for Fitting	Estimated Values ( $\mu\text{m}$ )		
			Tri-axes Ellipsoid		Fitting Error (%)
AR = 1:2	$a = 6.93$	0–43°	$q_1 = 6.93$	5.83	0.48
	$a = 6.93$		$q_2 = 5.59$	6.93	
	$b = 3.46$		$q_3 = 3.46$	3.46	
AR = 1:4	$a = 8.72$	0–35°	$q_1 = 8.74$	7.70	0.23
	$a = 8.72$		$q_2 = 8.90$	8.74	
	$b = 2.18$		$q_3 = 2.14$	2.14	
AR = 1:8	$a = 10.96$	0–28°	$q_1 = 10.95$	10.41	0.08
	$a = 10.96$		$q_2 = 10.19$	10.95	
	$b = 1.37$		$q_3 = 1.39$	1.39	
AR = 2:1	$a = 4.36$	90–114°	$q_1 = 4.38$	3.84	0.26
	$a = 4.36$		$q_2 = 5.27$	4.38	
	$b = 8.72$		$q_3 = 8.67$	8.67	
AR = 4:1	$a = 3.46$	90–108°	$q_1 = 3.46$	2.85	0.10
	$a = 3.46$		$q_2 = 4.32$	3.46	
	$b = 13.86$		$q_3 = 13.86$	13.86	
AR = 8:1	$a = 2.75$	90–102°	$q_1 = 2.75$	2.75	0.10
	$a = 2.75$		$q_2 = 1.89$	2.75	
	$b = 22.01$		$q_3 = 22.01$	22.01	

<sup>a</sup>Note that the curve fitting error is defined as fitting error =  $\frac{\|10 \log_{10}[\frac{\sigma(k, \theta)}{\sigma(k, \theta_m)}] - 10 \log_{10}[\frac{FF^2(k, \theta)}{FF^2(k, \theta_m)}]\|}{\|10 \log_{10}[\frac{\sigma(k, \theta)}{\sigma(k, \theta_m)}]\|} \times 100\%$ ;  $\|\cdot\|$  refers to the Euclidean norm and  $\theta$  varied from  $\theta_m$  (where DPACS became maximum) to the first minimum in the increasing  $\theta$  direction. Fitting error was found to be the same in both the directions ( $\phi = 0$  and  $90^\circ$ ).

and  $q_2$  agree well with the nominal values (deviation is  $\approx 4\%$ ). The estimated value of  $q_3$  lies between  $t = 1.4$  and  $b = 2.84 \mu\text{m}$ . The extracted value of  $\Gamma$  (Rows 4 and 5, Column 7) is close to the physical value (error  $\approx 2\%$ ) and  $L$  is comparable with the average thickness of the cell ( $\approx 2.14 \mu\text{m}$ ). Both models display a close match to the simulated DPACS curves up to the first minimum for Stomatocyte1 and Stomatocyte2 (see middle and lower panels of Fig. 8, respectively). However, the fittings are not good at the large angles (approximately between  $40^\circ$  and  $140^\circ$ ). The models slightly overestimate the dimension along the  $x$  axis/ $y$  axis of Stomatocyte1 by 18% and 20%, respectively. This is also true for the other cell. It is not straightforward to correlate the actual and determined values of the

third dimension owing to the complexity of shapes for the deformed cells. Moreover, a fitting error did not change when  $q_3$  varied from 0.1 to 0.5  $\mu\text{m}$  with an increment of 0.01  $\mu\text{m}$  for Stomatocyte2. The same was observed for  $L$ , too. That is why it is written as not converging in Table 4.

In this work, the PA fields have been calculated for non-spherical axisymmetric particles. This was accomplished by solving the time-independent wave equation by Green's function method. It provides an integral solution to the wave equation. The integration in this work was carried out using the Monte Carlo technique. The accuracy of this numerical method can be checked by comparing numerical and analytical results for the case of a homogeneous spherical source. It has been observed that it is a fast method and facilitates accurate results (data not shown). As stated earlier, we simulated pressure signals in the k-Wave toolbox from different RBCs with an initial pressure of unit strength and power at 390 MHz (denoted as  $|M(k)|^2$  in Fig. 6) was subsequently calculated for each shape. The power as a function of measurement angle was plotted to qualitatively match with the corresponding DPACS curve. The k-Wave toolbox does not allow us to control the magnitude of incident light intensity ( $I_0$ ); rather, an initial pressure rise has to be given as an input. Therefore, it was not possible to compute  $\sigma$  for this method, as the magnitude of  $I_0$  was not available, and difference (or error) between the k-Wave and Green's function results could not be obtained as well. Moreover, Green's function method works well because the condition of impedance matching has been imposed. However, impedance for RBCs approximately differ from the saline water by 16%; in that case, this method may not

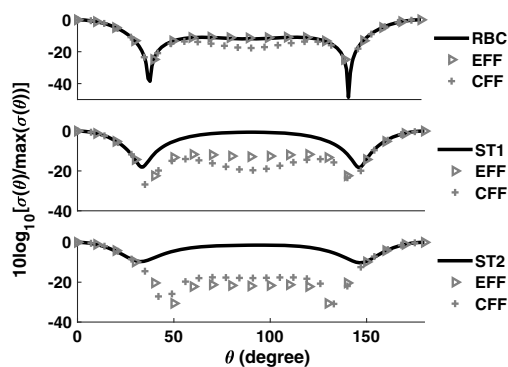


**Fig. 8.** Fitting of the angular distribution of the normalized DPACSs with the form factor models. Here, EFF refers to the tri-axes ellipsoid form factor; CFF indicates the finite cylinder form factor; ST1 and ST2 denote Stomatocyte1 and Stomatocyte2, respectively.

**Table 4.** Comparison between the Actual and the Evaluated Values of the Morphological Parameters for Normal and Pathological RBCs<sup>a</sup>

PA Source	Nominal Values ( $\mu\text{m}$ )	Angular Range for Fitting	Estimated Values ( $\mu\text{m}$ )				
			Tri-axes Ellipsoid			Finite Cylinder	
			$\phi = 0^\circ$	$\phi = 90^\circ$	Fitting Error (%)	Estimates	Fitting Error (%)
Normal RBC	$R_e = 3.82$	0–38°	$Q_1 = 3.65$	2.83	0.13	$\Gamma = 3.74$	1.0
	$t/2 = 0.7$		$Q_2 = 4.10$	3.65		$L = 2.19$	
	$b/2 = 1.42$		$Q_3 = 1.88$	1.88			
Stomatocyte1	$R_e = 3.18$	0–34°	$Q_1 = 3.76$	4.61	2.0	$\Gamma = 3.81$	1.8
	$t/2 = 1.36$		$Q_2 = 2.43$	3.76		$L = 2.11$	
	$b/2 = 1.47$		$Q_3 = 1.82$	1.82			
Stomatocyte2	$R_e = 3.27$	0–33°	$Q_1 = 3.67$	4.87	6.6	$\Gamma = 3.24$	7.4
	$t/2 = 0.21$		$Q_2 = 2.07$	3.67		$L = \text{Not}$	
	$b/2 = 1.16$		$Q_3 = \text{Not}$ converging	Not converging		converging	

<sup>a</sup>Note that the curve fitting error is defined as fitting error =  $\frac{\|10 \log_{10}[\frac{f(\vec{k}, \theta)}{\sigma(\vec{k}, \theta_m)}] - 10 \log_{10}[\frac{\text{FF}^2(\vec{k}, \theta)}{\text{FF}^2(\vec{k}, \theta_m)}]\|}{\|10 \log_{10}[\frac{\sigma(\vec{k}, \theta)}{\sigma(\vec{k}, \theta_m)}]\|} \times 100\%;$   $\|\cdot\|$  refers to the Euclidean norm and  $\theta$  varied from  $\theta_m$  (where DPACS became maximum) to the first minimum in the increasing  $\theta$  direction. Fitting error was found to be the same in both the directions ( $\phi = 0$  and  $90^\circ$ ).

work faithfully. Therefore, improved methods need to be devised to address this issue.

Figures 4(a) and 4(c) reveal that the surface area perpendicular to the direction of measurement determines the magnitude of the DPACS. It increases as the surface area increases. It is expected because the number of point sources emitting the PA fields and interfering constructively at the detector location (which is far away from the PA source) grows as the geometrical cross-sectional area increases, causing the DPACS to be high. On the other hand, it can be observed that the DPACS diminishes, as the thickness of the source along the direction of measurement increases. It may be speculated that an increase in thickness promotes incoherent addition of fields from point sources resulting in the DPACS to be low. It may also appear that these statements are not always valid [e.g., the DPACS for 1:8 (solid line) is higher than 1:4 (dashed-dotted line) at  $\theta = 90^\circ$  in Fig. 4(a)]. This is due to the fact that the curves exhibit oscillatory patterns. Additionally, such statements may better hold for envelopes (not shown in the figures) of those curves.

It is evident from Fig. 5(a) as well as from Fig. 6 that the DPACS attains its maximum when it is measured from  $\theta = 0^\circ$  for normal RBC. It looks like a thin disc when viewed from this direction. The maximum thickness of healthy RBC is about  $b = 2.84 \mu\text{m}$ , which is less than the wavelength ( $3.75 \mu\text{m}$ ) of interest; therefore, coherent addition of PA fields by points sources significantly increases along  $\theta = 0^\circ$ . Nevertheless, the maximum thickness becomes  $D = 7.65 \mu\text{m}$  when probed from  $\theta = 90^\circ$ ; therefore, some PA fields meet out of phase, reducing the magnitude of the DPACS. As in the previous case, along  $\theta = 0^\circ$ ,  $\sigma$  decreases as the cross-sectional area normal along this direction decreases. Nevertheless, the corresponding trend is not followed along  $\theta = 90^\circ$ . This is because RBC shapes are not simple. Moreover, an angular profile of the DPACS would lose its features (i.e., maxima and minima) if detection is performed at a lower frequency. For instance, the first minimum for normal RBC starts to appear within the angular domain at 200 MHz and the same for pathological RBCs becomes visible above

250 MHz. No minimum will be noticeable for RBCs if measurements are carried out below 200 MHz.

The form factor models have been successfully employed in different branches of science and engineering to analyze light, x-ray, and neutron scattering data to determine scatterer size. In that context, FF is a function of  $q\sigma$ , where  $\mathbf{q} = \mathbf{k}_s - \mathbf{k}_i$  is the momentum transfer with  $\mathbf{k}_i$  and  $\mathbf{k}_s$  the incident and scattered wave vectors, respectively; consequently,  $\text{FF} \rightarrow 1$  in the forward direction because  $q\sigma \rightarrow 0$  in this direction. However, the analogous situation did not arise in the case of PA emission at least for the acoustic frequencies considered in this study. The shape parameters were estimated precisely for spheroidal droplets and normal RBC. The extracted values for thickness parameters exhibited greater variability for pathological RBCs. Along with the best fit parameters, we also applied a fit process on the data, and the parameters of the fit were retrieved with uncertainties. Essentially, we stored all the combinations of values ( $Q_1, Q_2, Q_3$ ) or  $(Q_1, Q_2, Q_3)/(\Gamma, L)$  for which absolute fitting errors were  $\leq 5\%$ . After that, mean and standard deviation were obtained for each shape parameter (data not shown). It was found that the uncertainty in each measurement for spheroidal particles remains below 10%, and that is why precise estimation was accomplished. A similar study carried out for normal RBC demonstrated that standard deviation in general in each case remains to be  $< 10\%$ . However, for deformed RBCs, standard deviations along the  $z$  axis approach to 50%, showing that the estimates in this direction are erroneous. More robust methods may be developed in the future to accurately fit the DPACS curves, particularly for deformed RBCs and, consequently, obtain estimates for clinical usage. Furthermore, in this work, we considered axisymmetric shapes only. In the future, nonaxisymmetric shapes, particularly echinocyte states of RBC, would be considered. Hence, it would be interesting to construct nonspherical nonaxisymmetric shapes using spherical harmonic expansion [35,36] and examine how DPACS would vary with angle (both polar and azimuthal) for such shapes. It would also be interesting to investigate how form factor models would work assessing characteristic sizes of diseased cells.

## 4. CONCLUSIONS

In conclusion, an expression for the DPACS in terms of form factor is derived. Variation of the DPACSS with polar angles for spheroidal droplets and normal and pathological RBCs have been investigated and also fitted with form factor models to determine shape parameters. It is found that the DPACS increases as the surface area of the PA source perpendicular to the direction of measurement increases and decreases as the thickness of the source along the same direction increases. For example, the DPACS along the symmetry axis grows by 20-fold when the surface area is increased by 44% (from Stomatocyte1 to normal RBC). Further, angular positions of minima also depend on cellular size and shape. The tri-axes form factor model provided accurate estimates of shape parameters for spheroidal droplets. Morphology of normal RBC was evaluated with  $\approx 4\%$  accuracy using the tri-axes and finite cylinder form factor models. This study may guide design experiments to measure angular distribution of the DPACS and, accordingly, to assess cellular morphology by optimizing experimental and theoretical data.

**Acknowledgment.** Stimulating discussion with Pankaj Warbal and Ravi Prakash is gratefully acknowledged. The authors would like to sincerely thank the anonymous reviewer for his/her comments, which helped us to improve the quality of the paper to a great extent. Special thanks to the members of the Systems Laboratory, IIITA for providing HPC facility.

## REFERENCES

- P. Beard, "Biomedical photoacoustic imaging," *Interface Focus* **1**, 602–631 (2011).
- H. F. Zhang, K. Maslov, G. Stoica, and L. V. Wang, "Functional photoacoustic microscopy for high-resolution and noninvasive in vivo imaging," *Nat. Biotechnol.* **24**, 848–851 (2006).
- L. V. Wang and S. Hu, "Photoacoustic tomography: in vivo imaging from organelles to organs," *Science* **335**, 1458–1462 (2012).
- V. Ntziachristos, "Going deeper than microscopy: the optical imaging frontier in biology," *Nat. Methods* **7**, 603–614 (2010).
- J. Weber, P. C. Beard, and S. E. Bohndiek, "Contrast agents for molecular photoacoustic imaging," *Nat. Methods* **13**, 639–650 (2016).
- G. He, B. Li, and S. Yang, "In vivo imaging of a single erythrocyte with high-resolution photoacoustic microscopy," *Front. Optoelectron.* **8**, 122–127 (2015).
- E. M. Strohm, E. S. L. Berndl, and M. C. Kolios, "Probing red blood cell morphology using high frequency photoacoustics," *Biophys. J.* **105**, 59–67 (2013).
- E. M. Strohm, E. S. L. Berndl, and M. C. Kolios, "High frequency label-free photoacoustic microscopy of single cells," *Photoacoustics* **1**, 49–53 (2013).
- G. J. Diebold, T. Sun, and M. I. Khan, "Photoacoustic monopole radiation in one, two and three dimensions," *Phys. Rev. Lett.* **67**, 3384–3387 (1991).
- R. K. Saha and M. C. Kolios, "A simulation study on photoacoustic signals from red blood cells," *J. Acoust. Soc. Am.* **129**, 2935–2943 (2011).
- R. K. Saha and M. C. Kolios, "Effects of erythrocyte oxygenation on optoacoustic signals," *J. Biomed. Opt.* **16**, 115003 (2011).
- R. K. Saha, S. Karmakar, and M. Roy, "Computational investigation on the photoacoustics of malaria infected red blood cells," *PLoS ONE* **7**, e51774 (2012).
- R. K. Saha, "Computational modeling of photoacoustic signals from mixtures of melanoma and red blood cells," *J. Acoust. Soc. Am.* **136**, 2039–2049 (2014).
- E. Hysi, R. K. Saha, and M. C. Kolios, "Photoacoustic ultrasound spectroscopy for red blood cell aggregation and oxygenation," *J. Biomed. Opt.* **17**, 125006 (2012).
- R. K. Saha, S. Karmakar, and M. Roy, "Photoacoustic response of suspended and hemolyzed red blood cells," *Appl. Phys. Lett.* **103**, 044101 (2013).
- Y. Li and H. Fang, "Photoacoustic pulse wave forming along the rotation axis of an ellipsoid droplet: a geometric calculation study," *Appl. Opt.* **52**, 8258–8269 (2013).
- Y. Li, H. Fang, C. Min, and X. Yuan, "Analytic theory of photoacoustic wave generation from a spheroidal droplet," *Opt. Express* **22**, 19953–19969 (2014).
- B. E. Treeby and B. T. Cox, "k-Wave: MATLAB toolbox for the simulation and reconstruction of photoacoustic wave fields," *J. Biomed. Opt.* **15**, 021314 (2010).
- R. K. Saha, S. Karmakar, A. Adhikari, and M. C. Kolios, "Photoacoustic field calculation for nonspherical axisymmetric fluid particles," *Biomed. Phys. Eng. Express* **3**, 015017 (2017).
- N. Uluc, M. B. Unlu, G. Gulsen, and H. Erkol, "Extended photoacoustic transport model for characterization of red blood cell morphology in microchannel flow," *Biomed. Opt. Express* **9**, 2785–2809 (2018).
- J. Jung, L. E. Matemba, K. Lee, P. E. Kazyoba, J. Yoon, J. J. Massaga, K. Kim, D. J. Kim, and Y. Park, "Optical characterization of red blood cells from individuals with sickle cell trait and disease in Tanzania using quantitative phase imaging," *Sci. Rep.* **6**, 31698 (2016).
- Y. Katsumoto, K. Tatsumi, T. Doi, and K. Nakabe, "Electrical classification of single red blood cell deformability in high-shear microchannel flows," *Int. J. Heat Fluid Flow* **31**, 985–995 (2010).
- C. Alves and C. L. P. Oliveira, *Calculation of Small-Angle Scattering Patterns* (IntechOpen, 2018), Chap. 1.
- M. A. Schroer, "Small angle X-ray scattering studies on proteins under extreme conditions," Ph.D. thesis (TU Dortmund, 2011), Chap. 2.
- N. Skar-Gislinge and L. Arleth, "Small-angle scattering from phospholipid nanodiscs: derivation and refinement of a molecular constrained analytical model form factor," *Phys. Chem. Chem. Phys.* **13**, 3161–3170 (2011).
- R. K. Saha, "A simulation study on the quantitative assessment of tissue microstructure with photoacoustics," *IEEE Trans. Ultrason. Ferroelectr. Freq. Control* **62**, 881–895 (2015).
- P. M. Morse and H. Feshbach, *Methods of Theoretical Physics* (McGraw-Hill, 1953), Chap. 7, pp. 791–895.
- L. Bi and P. Yang, "Modeling of light scattering by biconcave and deformed red blood cells with the invariant imbedding T-matrix method," *J. Biomed. Opt.* **18**, 055001 (2013).
- H. W. G. Lim, M. Wortis, and R. Mukhopadhyay, "Stomatocyte-discocyte-echinocyte sequence of the human red blood cell: Evidence for the bilayer-couple hypothesis from membrane mechanics," *Proc. Natl. Acad. Sci. USA* **99**, 16766–16769 (2002).
- W. H. Reinhart and S. Chien, "Red cell rheology in stomatocyte-echinocyte transformation roles of cell geometry and cell shape," *Blood* **67**, 1110–1118 (1986).
- M. Toubal, M. Asmani, E. Radziszewski, and B. Nongaillard, "Acoustic measurement of compressibility and thermal expansion coefficient of erythrocytes," *Phys. Med. Biol.* **44**, 1277–1287 (1999).
- S. Prahl, "Optical absorption of hemoglobin," 2018, <https://omlc.org/spectra/hemoglobin/>.
- M. F. Perutz, "The hemoglobin molecule," *Sci. Am.* **211**, 64–76 (1964).
- H. Funaki, "Contributions on the shapes of red blood corpuscles," *Jpn. J. Physiol.* **5**, 81–92 (1955).
- K. Khairy and J. Howard, "Spherical harmonics-based parametric deconvolution of 3D surface images using bending energy minimization," *Med. Image Anal.* **12**, 217–227 (2008).
- K. Khairy, J. Foo, and J. Howard, "Shapes of red blood cells: comparison of 3D confocal images with the bilayer-couple model," *Cell Mol. Bioeng.* **1**, 173–181 (2010).
- M. Pharr and G. Humphreys, *Physically Based Image Synthesis: from Theory to Implementation* (Elsevier, 2004), Chap. 14, pp. 497–520.